PAPER

Check for updates

Pt nanoparticle dispersed Ni(OH)$_2$ nanosheets via a pulsed laser deposition method efficiently enhanced hydrogen evolution reaction performance in alkaline conditions †

Zhong Zhao, [ab] Shengbo Zhang, [ba] Meng Jin [*ba] and Haimin Zhang [*ba]

The use of electrochemical water is a very attractive and environmentally friendly solution for hydrogen fuel production. Platinum (Pt) catalysts are considered to be the most active catalyst for the hydrogen evolution reaction (HER) but suffer from low efficiency and slow kinetics. Herein, Pt nanoparticles dispersed Ni(OH)$_2$ nanosheets (Pt–Ni(OH)$_2$-X) with different deposition times were designed and developed via a vapour-phase hydrothermal method, followed by a pulsed laser deposition method. The Pt–Ni(OH)$_2$-5 only needs overpotentials of 247.5 ± 43 and 512.5 ± 18 mV to reach current densities of 10 and 100 mA cm^{-2}, respectively, outperforming the commercial Pt/C at a current density of 100 mA cm^{-2}. Furthermore, the infrared spectrum revealed that the adsorption of water molecules becomes stronger at the surface of the Pt–Ni(OH)$_2$-5 nanosheets, and the hydrogen protons overflow onto the Pt surface and facilitate the HER process. This work suggests that moderate Pt nanoparticle dispersed Ni(OH)$_2$ nanosheet help to promote the hydrogen production process.

Introduction

Hydrogen is considered to be the most promising source of energy due to it having zero carbon and a high energy density. Compared with the cost problems associated with an acidic solution, the electrochemical hydrogen evolution reaction (HER) in an alkaline medium has attracted extensive attention.[1,2] However, due to the high activation energy of the water dissociation step ($H_2O + e^- \rightarrow OH^- + H^*$) in alkaline HER, the reaction kinetics were much slower, in fact 2–3 orders of magnitude lower than those in an acidic solution.[3] Platinum-based (Pt-) catalysts are the most widely studied and used catalysts in electrochemical hydrogen production. In an alkaline medium, the platinum–hydrogen adsorbate (Pt–H$_{ads}$) was formed by water dissociation rather than the hydronium ion in an acidic medium, and was hampered by the prior water-dissociation step.[4] Moreover, they often suffered from scarcity and high costs.[5,6] Therefore, it is urgent to develop a high activity and high stability.

Recently, transition metal hydroxides have attracted a great deal of attention because the oxygen-philic surface is beneficial

for water splitting.[7,8] In addition, the interaction energy between the hydroxyl ion (OH$^-$) and $M^{2+\delta}O^{\delta}(OH)_{2-\delta}$ (OH$^- \leftrightarrow OH_{ad}$–$M^{2+\delta}O^{\delta}(OH)_{2-\delta}$, where M = metal) can be effectively weakened by combining Pt with transition metal hydroxides, thus promoting the desorption of OH$^-$.[7] Among them, the Ni(OH)$_2$ with the lowest OH_{ad}–$M^{2+\delta}O^{\delta}(OH)_{2-\delta}$ energy is the best carrier for Pt loading.[9] For example, Belcher and co-workers fabricated Pt–Ni(OH)$_2$ nanonetworks, possessing high activity via a simple synthesis method for bacteriophage templating. In 1 M KOH, the materials displayed -4.9 A mg^{-1} Pt at -70 mV versus the reversible hydrogen electrode (RHE).[10] Gu et al. successfully synthesised a Pt–Ni(OH)$_2$ hybrid in situ on anodised nickel foam via a hydrothermal decomposition method.[11] At the current densities of 10 and 100 mA cm^{-2}, the overpotentials were only 25.9 mV and 211 mV, respectively, which showed excellent performance for alkaline HER. The Pt nanodots on Pt/Ni(OH)$_2$/NF-A promote the H adsorption and further improve the HER mass activity.[12] Zhao et al. designed the Pt@Ni–Ni(OH)$_2$ nanotube array heterostructure and achieved a lower overpotential of 27 mV at 10 mA cm^{-2}.[7] In a high-alkaline solution, the low-energy peak of Ni 2p$_{3/2}$ is oxidised to Ni^{2+}, thus promoting the HER performance. Based on the laser ablation process, the pulsed laser deposition (PLD) method was an important method for preparing high-quality nanoparticles.[13] Therefore, it is of great significance to prepare a Pt–Ni(OH)$_2$ catalyst with high performance and low Pt loading based on the PLD method.

Based on the previous discussion, we fabricated a Pt nanoparticle dispersed Ni(OH)$_2$ nanosheet catalyst with different

[a]University of Science and Technology of China, Hefei 230026, China

[b]Key Laboratory of Materials Physics, Institute of Solid State Physics, HFIPS, Chinese Academy of Sciences, Hefei 230031, China. E-mail: zhanghm@issp.ac.cn; mjin1992@mail.ustc.edu.cn

deposition times (Pt–Ni(OH)$_2$-X, where X represents the deposition time) using a vapour-phase hydrothermal (VPH) method and a PLD method. The Pt–Ni(OH)$_2$-5 sample exhibited good performance in 1 M KOH (pH 14). The Tafel slope was 212.5 ± 30 mV dec^{-1}, and the overpotentials were 247.5 ± 43 and 512.5 ± 18 mV at the current densities of 10 and 100 mA cm^{-2}, respectively. The Fourier transform infrared spectroscopy (FTIR) results revealed that the adsorption of the water molecules can be boosted at the Ni(OH)$_2$ surface and this favours the following hydrogen production process.

Results and discussion

The Pt nanoparticle dispersed Ni(OH)$_2$ nanosheets (Pt–Ni(OH)$_2$-X) with different deposition times were developed using the VPH method followed by the PLD method. Typically, the Ni(OH)$_2$ nanosheet on the Ni foam was prepared by a simple, easy VPH method as shown in Fig. 1a.[14] The X-ray diffraction (XRD) patterns were used for confirming the presence of crystalline phases. The characteristic peaks at 11.3°, 22.7°, 33.5°, 34.4°, 38.8°, 46.0°, 60.0°, 61.3° can be indexed to the (003), (006), (101), (012), (015), (018), (110), (113) planes of α-Ni(OH)$_2$ (PDF#38-0715), respectively, (Fig. 1b). The other characteristic peaks at 19.3°, 33.0°, 38.5°, 39.0°, 52.1° are characteristic of the β-Ni(OH)$_2$ planes (PDF#14-0117). The XRD results demonstrated that the Ni(OH)$_2$ nanosheet was composed of two different phases, which coexisted together. In addition, scanning electron microscopy (SEM) showed that all the Ni(OH)$_2$ nanosheets are uniformly dense on top of the nickel foam, and clearly demonstrated a change in morphology of the materials

obtained, which were deposited at different times (Fig. 1c and S1 ESI†). With the increase of deposition time, the Ni(OH)$_2$ nanosheets gradually become amorphous structures (Fig. S1, ESI†). Furthermore, different deposition thicknesses of Pt nanoparticles dispersed on Ni(OH)$_2$ nanosheets were fabricated using the PLD method (denoted as Pt–Ni(OH)$_2$-X, where $X = 0$, 2.5, 5, 7.5, or 10 min) and the corresponding fabrication method is shown in Fig. S2 (ESI†). The TEM images show that Pt–Ni(OH)$_2$-5 was formed by a rough lump of β-Ni(OH)$_2$ and lamellar α-Ni(OH)$_2$, which is consistent with the XRD results (Fig. 1b). In addition, the Pt nanoparticles were unambiguously identified on the Ni(OH)$_2$ nanosheet. It is important to note that the STEM-EDX elemental mapping revealed that Ni, O, and Pt were uniformly distributed, and the Pt species were uniformly dispersed on the Ni(OH)$_2$ (Fig. 1d). Furthermore, the high-resolution transmission electron microscopy (HRTEM) image (Fig. 1e) shows that the lattice spacing of 0.196, 0.197, 0.227, 0.23 nm corresponds to the Pt(200), α-Ni(OH)$_2$(018), Pt(111), β-Ni(OH)$_2$(002) planes, respectively.

These results demonstrated that the Pt species was successfully dispersed on the Ni(OH)$_2$ nanosheets without changing its crystal structure. The Pt-dispersed Ni(OH)$_2$ nanosheets with different Pt loading contents was analysed by inductively coupled plasma – atomic emission spectroscopy. The Pt loading contents were 0.00522 ± 0.00155, 0.01062 ± 0.00184, 0.0196 ± 0.00126, 0.03199 ± 0.00647 mg cm^{-2} for Pt–Ni(OH)$_2$-2.5, Pt–Ni(OH)$_2$-5, Pt–Ni(OH)$_2$-7.5, Pt–Ni(OH)$_2$-10, respectively. The surface properties were further investigated using Brunauer–Emmett–Teller (BET) gas sorption measurements. The nitrogen adsorption–desorption isotherm, and the pore-size distributions of the Ni(OH)$_2$ electrocatalyst are shown in Fig. S3 (ESI†). The surface areas were found to be 53 m^2 g^{-1}. The higher BET surface area of the Ni(OH)$_2$ would enhance the mass transport of the electrocatalytic reactions, and could be used as a stable HER electrocatalysis support.[15,16]

The X-ray photoelectron spectroscopy (XPS) was used to further investigate the chemical compositions and chemical valence of the Ni, O, and Pt elements (Fig. 2a). The spectra of Ni 2p for Ni(OH)$_2$, Pt–Ni(OH)$_2$-5 and Pt–Ni(OH)$_2$-5 after stability testing are shown in Fig. 2b. The peaks of Ni(OH)$_2$ at about 855.8 and 873.5 are assigned to Ni^{2+} 2p$_{3/2}$, and Ni^{2+} 2p$_{1/2}$, respectively.[17–19] Peaks located at 880.3 and 862.4 eV are assigned to the two satellite peaks. For Pt–Ni(OH)$_2$-5, the peaks at 855.8 and 873.5 eV show slightly negative shifts of approximately 1.05 eV when compared with the Ni(OH)$_2$ Ni^{2+} 2p$_{3/2}$ peak, and a positive shift of approximately 0.05 eV compared with the Ni(OH)$_2$ Ni^{2+} 2p$_{1/2}$ peak. Compared with Pt 4f, the peaks of Pt–Ni(OH)$_2$-5 were shifted to a lower binding energy (Fig. 2c). The previous results indicate that in partial electron transfer between Pt and Ni(OH)$_2$, Ni was the electron donor whereas Pt was an electron acceptor.[20] After the deposition of Pt, the local electron configuration of Ni(OH)$_2$ was regulated, which may be conducive to the subsequent alkaline HER process. For the O 1s spectrum, the peaks at 530 and 531.2 eV can be deconvoluted into metal–oxygen peaks and surface-adsorbed oxygen (Fig. 2d). The O 1s signal in Pt–Ni(OH)$_2$-5 shows a slight positive shift
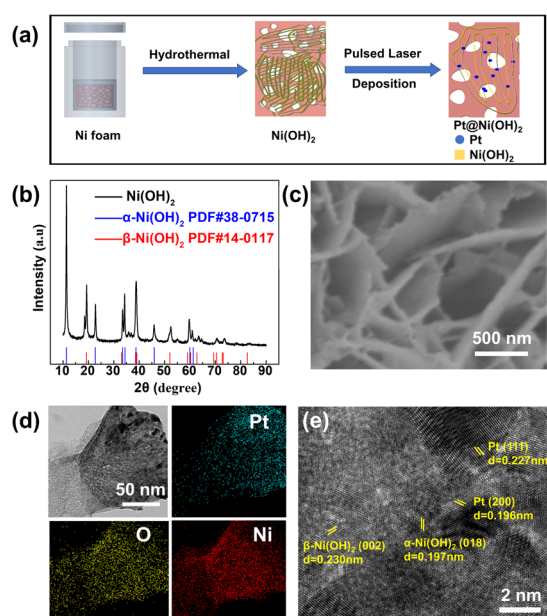

Fig. 1 (a) Diagram of the Pt–Ni(OH)$_2$-X synthesis process. (b) XRD patterns of Ni(OH)$_2$, α-Ni(OH)$_2$, β-Ni(OH)$_2$. (c) SEM image of the Pt–Ni(OH)$_2$-5 sample. (d) STEM and corresponding EDX element mapping of image of the Pt–Ni(OH)$_2$-5 sample. (e) HRTEM of the Pt–Ni(OH)$_2$-5 sample.
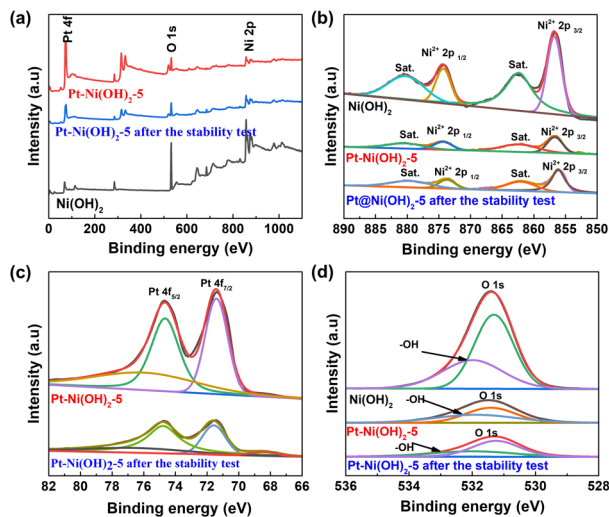
Fig. 2 (a) XPS survey spectra of Pt–Ni(OH)$_2$-5, Pt–Ni(OH)$_2$-5 after the stability test, and Ni(OH)$_2$. High-resolution XPS spectra (b) Ni 2p of Ni(OH)$_2$ and Pt–Ni(OH)$_2$-5, and Pt–Ni(OH)$_2$-5 after the stability test. (c) Pt 4f of Pt–Ni(OH)$_2$-5, and Pt–Ni(OH)$_2$-5 after the stability test. (d) O 1s of Ni(OH)$_2$ and Pt–Ni(OH)$_2$-5, and Pt–Ni(OH)$_2$-5 after the stability test.

relative to that of Ni(OH)$_2$, which is attributed to the strong electronic interaction between Pt and the Ni(OH)$_2$ support.

The electrocatalytic HER performance of Pt–Ni(OH)$_2$-X in 1 M KOH (pH = 14) solution with infrared (IR) correction was measured in a typical three-electrode H-type configuration (Fig. S4, ESI†). For comparison, Pt/C (60 wt%), Ni(OH)$_2$, Pt–Ni(OH)$_2$-2.5, Pt–Ni(OH)$_2$-5, Pt–Ni(OH)$_2$-7.5, Pt–Ni(OH)$_2$-10, were also measured under the same conditions, and the linear sweep voltammetry (LSV) curves are shown in Fig. 3a. The over-potentials of Pt/C (60 wt%), Ni(OH)$_2$, Pt–Ni(OH)$_2$-2.5, Pt–
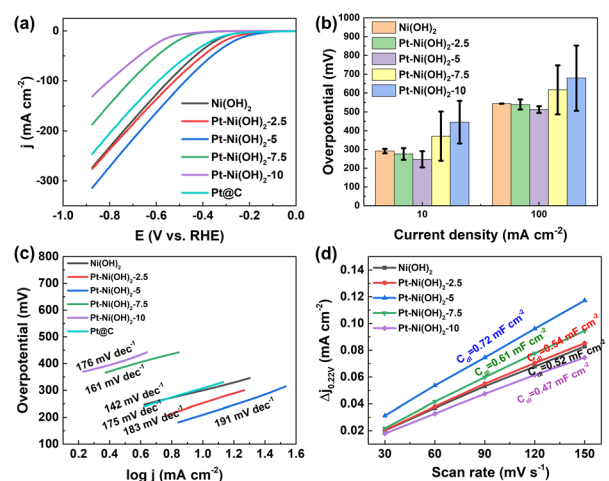
Ni(OH)$_2$-5, Pt–Ni(OH)$_2$-7.5, and Pt–Ni(OH)$_2$-10 at 10 mA cm^{-2} were 315, 291.5 ± 12, 276 ± 31, 247.5 ± 43, 371 ± 131, and 445.5 ± 114 mV, respectively (Fig. 3b). The Pt–Ni(OH)$_2$-5 displays a lower overpotential than the other electrocatalysts, but that of the Pt–Ni(OH)$_2$-5 (217 ± 61 mV) was superior to all the other Pt–Ni(OH)$_2$-X. At a higher current density of 100 mA cm^{-2}, the Pt–Ni(OH)$_2$-5 catalyst (512.5 ± 18 mV) exhibits an excellent alkaline HER activity when compared with that of Pt/C (60 wt%, 590 mV), which indicates that the Pt–Ni(OH)$_2$-5 catalyst has a better potential for future use in commercial applications than the Pt/C (60 wt%) at a higher current density. The Pt deposition on the Ni(OH)$_2$ can significantly enhance the electrocatalytic performance (Fig. 3b and S5, ESI†). The Tafel slope further clarified the hydrogen production reaction kinetics (Fig. 3c and S6, ESI†).[21] For the Pt–Ni(OH)$_2$-5, the slope of the Tafel plot was 212.5 ± 30 mV dec^{-1}, which was superior to those of the Ni(OH)$_2$ (166 ± 34 mV dec^{-1}), Pt–Ni(OH)$_2$-2.5 (192 ± 13 mV dec^{-1}), Pt–Ni(OH)$_2$-7.5 (172.5 ± 16 mV dec^{-1}), Pt–Ni(OH)$_2$-10 (159 ± 24 mV dec^{-1}). Generally, in alkaline electrolytes, the HER reaction pathway was achieved via a Tafel–Volmer–Heyrovsky mechanism (Scheme S1, ESI†).[22] Ideally, if the Volmer reaction is fast when the rate-limiting step is the Tafel reaction or the Heyrovsky reaction, a low Tafel slope of 29 or 38 mV dec^{-1} at 25 °C should be observed.[21] In contrast, the Tafel slope should be 116 mV dec^{-1} at 25 °C, meaning that the Volmer reaction was the limiting step.[23] The Tafel slope of 212.5 ± 30 mV dec^{-1} for Pt–Ni(OH)$_2$-5, indicated that the Volmer reaction was the dominant rate-limiting step. These results demonstrated faster electron transport and lower charge-transfer resistance on the Pt–Ni(OH)$_2$-5, which in turn facilitates electron transfer and is beneficial for the HER process. The electrochemical surface areas (ECSA) were investigated in depth to obtain the electrocatalyst's intrinsic activity information. Based on the cyclic voltammogram curves (CVs) at different scan rates, the double-layer capacitances (C_{dl}) were calculated (Fig. S7, ESI†). Fig. 3d shows that the C_{dl} of Pt–Ni(OH)$_2$-5 (0.72 mF cm^{-2}) was much larger than those of Ni(OH)$_2$ (0.52 mF cm^{-2}), Pt–Ni(OH)$_2$-2.5 (0.54 mF cm^{-2}), Pt–Ni(OH)$_2$-7.5 (0.61 mF cm^{-2}), and Pt–Ni(OH)$_2$-10 (0.47 mF cm^{-2}), indicating that the Pt–Ni(OH)$_2$-5 possesses more active sites at the three-phase reaction interface. Furthermore, long-term stability is considered to be an important parameter to evaluate the practical application of electrocatalysts.[24] As shown in Fig. S8 (ESI†), in the chronopotentiometry test, the current density of Pt–Ni(OH)$_2$-5 was

Fig. 3 (a) Polarisation curves of Pt@C, Ni(OH)$_2$, Pt–Ni(OH)$_2$-2.5, Pt–Ni(OH)$_2$-5, Pt–Ni(OH)$_2$-7.5, and Pt–Ni(OH)$_2$-10 for the HER in 1 M KOH with 95% IR-correction. (b) Homologous overpotential bar graph at 10 and 100 mA cm^{-2}, and (c) the corresponding Tafel plots of Pt@C, Ni(OH)$_2$, Pt–Ni(OH)$_2$-2.5, Pt–Ni(OH)$_2$-5, Pt–Ni(OH)$_2$-7.5, and Pt–Ni(OH)$_2$-10. (d) Polarisation curves normalised by the C_{dl} of Ni(OH)$_2$, Pt–Ni(OH)$_2$-2.5, Pt–Ni(OH)$_2$-5, Pt–Ni(OH)$_2$-7.5, and Pt–Ni(OH)$_2$-10.
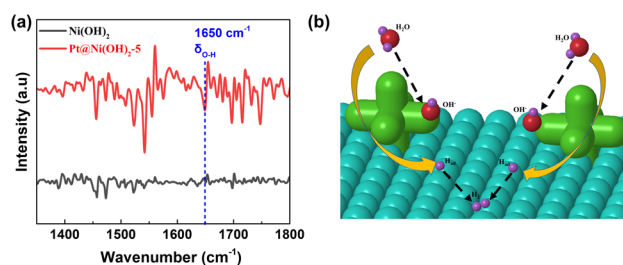

Fig. 4 (a) The FTIR spectra of Ni(OH)$_2$ and the Pt–Ni(OH)$_2$-5 sample. (b) A schematic diagram of the reaction mechanism on the Pt–Ni(OH)$_2$-5 sample.

not degraded, indicating that the electrocatalyst has good stability in 1 M KOH solution for at least 24 h. The FTIR was carried out to confirm the H_2O adsorption during the reaction process (Fig. 4a).[25] The strong peaks at 1650 cm^{-1} are attributed to the δ_{O-H} vibration peaks. Compared to $Ni(OH)_2$, Pt–$Ni(OH)_2$-5 displays stronger δ_{O-H} vibration peaks, signifying that the adsorption of OH$^-$ was significantly enhanced after Pt deposition, and the H$^+$ may overflow onto the Pt surface, where the two molecules combine to produce hydrogen (Fig. 4b).

Conclusions

In summary, different Pt nanoparticle contents were deposited on the $Ni(OH)_2$ via the vapour-phase hydrothermal method, followed by the pulsed laser deposition method. Notably, the Pt–$Ni(OH)_2$-5 electrode obtained exhibited a remarkable catalytic activity for the HER process in 1 M KOH electrolyte. The overpotential for Pt–$Ni(OH)_2$-5 was 247.5 ± 43 and 512.5 ± 18 mV at the current densities of 10, and 100 mA cm^{-2}, respectively, and the Tafel slope was 212.5 ± 30 mV dec^{-1}. The FTIR results revealed that Pt deposition increased the adsorption of OH$^-$ on $Ni(OH)_2$, and then produced hydrogen by the hydrogen overflow phenomenon.

Author contributions

HZ conceptualised the overall research objectives. ZZ prepared and characterised the materials, and tested the electrochemical measurements. SZ tested the infrared data and participated in the discussions. HZ and MJ supervised the work and co-wrote the manuscript. All the authors discussed the experimental results and commented on the manuscript.

Conflicts of interest

There are no conflicts to declare.

Acknowledgements

Notes and references

1 J. Kim, H. Jung, S. M. Jung, J. Hwang, D. Y. Kim, N. Lee, K. S. Kim, H. Kwon, Y. T. Kim, J. W. Han and J. K. Kim, Tailoring Binding Abilities by Incorporating Oxophilic Transition Metals on 3D Nanostructured Ni Arrays for Accelerated Alkaline Hydrogen Evolution Reaction, *J. Am. Chem. Soc.*, 2021, **143**(3), 1399–1408.

2 X. Lan, G. Li, R. Jin, X. Li and J. Zheng, Carbon coated nickel cobalt phosphide with sea urchin-like structure by Low Temperature Plasma Processing for Hydrogen Evolution and Urea Oxidation, *Chem. Eng. J.*, 2022, **450**, 138225.

3 Y. Zheng, Y. Jiao, A. Vasileff and S. Z. Qiao, The Hydrogen Evolution Reaction in Alkaline Solution: From Theory, Single Crystal Models, to Practical Electrocatalysts, *Angew. Chem., Int. Ed.*, 2018, **57**, 7568–7579.

4 B. Ruqia and S. I. Choi, Pt and Pt-$Ni(OH)_2$ Electrodes for the Hydrogen Evolution Reaction in Alkaline Electrolytes and Their Nanoscaled Electrocatalysts, *ChemSusChem*, 2018, **11**, 2643–2653.

5 L. Wang, Y. Hao, L. Deng, F. Hu, S. Zhao, L. Li and S. Peng, Rapid Complete Reconfiguration Induced Actual Active Species for Industrial Hydrogen Evolution Reaction, *Nat. Commun.*, 2022, **13**, 5785.

6 Q. Chen, B. Wei, Y. Wei, P. Zhai, W. Liu, X. Gu, Z. Yang, J. Zuo, R. Zhang and Y. Gong, Synergistic Effect in Ultrafine PtNiP Nanowires for Highly Efficient Electrochemical Hydrogen Evolution in Alkaline Electrolyte, *Appl. Catal., B*, 2022, **301**, 120754.

7 D. Li, F. Liu, J. Dou and Q. Zhao, Pt Decorated Ni–$Ni(OH)_2$ Nanotube Arrays for Efficient Hydrogen Evolution Reaction, *ChemCatChem*, 2021, **13**, 5078–5083.

8 H. C. Fu, X. H. Wang, X. H. Chen, Q. Zhang, N. B. Li and H. Q. Luo, Interfacial Engineering of $Ni(OH)_2$ on W_2C for Remarkable Alkaline Hydrogen Production, *Appl. Catal., B*, 2022, **301**, 120818.

9 R. Subbaraman, D. Tripkovic, K. C. Chang, D. Strmcnik, A. P. Paulikas, P. Hirunsit, M. Chan, J. Greeley, V. Stamenkovic and N. M. Markovic, Trends in Activity for the Water Electrolyser Reactions on 3d M (Ni, Co, Fe, Mn) Hydr(oxy)oxide Catalysts, *Nat. Mater.*, 2012, **11**, 550–557.

10 W. C. Records, Y. Yoon, J. F. Ohmura, N. Chanut and A. M. Belcher, Virus-templated Pt–$Ni(OH)_2$ Nanonetworks for Enhanced Electrocatalytic Reduction of Water, *Nano Energy*, 2019, **58**, 167–174.

11 Y. Gu, Y. Wang, J. Shi, M. Yang, Y. Rui, W. An and Y. Men, Well-dispersed Pt Nanodots Interfaced with $Ni(OH)_2$ on Anodized Nickel Foam for Efficient Hydrogen Evolution Reaction, *Int. J. Hydrogen Energy*, 2020, **45**, 27067–27077.

12 W. Sheng, Z. Zhuang, M. Gao, J. Zheng, J. G. Chen and Y. Yan, Correlating Hydrogen Oxidation and Evolution Activity on Platinum at Different pH with Measured Hydrogen Binding Energy, *Nat. Commun.*, 2015, **6**, 5848.

13 A. A. Menazea and A. M. Mostafa, Ag doped CuO Thin Film Prepared via Pulsed Laser Deposition for 4-nitrophenol Degradation, *J. Environ. Chem. Eng.*, 2020, **8**, 104104.

14 M. Jin, X. Zhang, X. Zhang, H. Zhou, M. Han, Y. Zhang, G. Wang and H. Zhang, Interfacial Engineering of Metallic Rhodium by Thiol Modification Approach for Ambient Electrosynthesis of Ammonia, *Nano Res.*, 2022, **15**, 8826–8835.

15 J. Zhu, Z. Wang, H. Yu, N. Li, J. Zhang, J. Meng, M. Liao, J. Zhao, X. Lu, L. Du, R. Yang, D. Shi, Y. Jiang and G. Zhang, Argon Plasma Induced Phase Transition in Monolayer MoS_2, *J. Am. Chem. Soc.*, 2017, **139**, 10216–10219.

16 R. Ding, Q. Chen, Q. Luo, L. Zhou, Y. Wang, Y. Zhang and G. Fan, Salt Template-assisted in situ Construction of Ru Nanoclusters and Porous Carbon: Excellent Catalysts toward Hydrogen Evolution, Ammonia-Borane Hydrolysis, and 4-Nitrophenol Reduction, *Green Chem.*, 2020, **22**, 835–842.

17 Q. Zong, H. Yang, Q. Wang, Q. Zhang, Y. Zhu, H. Wang and Q. Shen, Three-dimensional Coral-like NiCoP@C@Ni(OH)$_2$ Core-shell Nanoarrays as Battery-Type Electrodes to Enhance Cycle Stability and Energy Density for Hybrid Supercapacitors, *Chem. Eng. J.*, 2019, **361**, 1–11.

18 Y. Liu, N. Fu, G. Zhang, M. Xu, W. Lu, L. Zhou and H. Huang, Design of Hierarchical NiCo@NiCo Layered Double Hydroxide Core-Shell Structured Nanotube Array for High-Performance Flexible All-Solid-State Battery-Type Supercapacitors, *Adv. Funct. Mater.*, 2017, **27**, 1605307.

19 Y. Wang, F. Cao, W. Lin, F. Zhao, J. Zhou, S. Li and G. Qin, *In Situ* Synthesis of Ni/NiO Composites with Defect-Rich Ultrathin Nanosheets for Highly Efficient Biomass-Derivative Selective Hydrogenation, *J. Mater. Chem. A*, 2019, **7**, 17834–17841.

20 Z. Fang, P. Wu, Y. Qian and G. Yu, Gel-Derived Amorphous BiNi Alloy Promotes Electrocatalytic Nitrogen Fixation *via* Optimizing Nitrogen Adsorption and Activation, *Angew. Chem., Int. Ed.*, 2021, **60**, 4275.

21 H. Li, P. Wen, Q. Li, C. Dun, J. Xing, C. Lu, S. Adhikari, L. Jiang, D. L. Carroll and S. M. Geyer, Earth-Abundant Iron Diboride (FeB$_2$) Nanoparticles as Highly Active Bifunctional Electrocatalysts for Overall Water Splitting, *Adv. Energy Mater.*, 2017, **7**, 1700513.

22 X. Lu, M. Cai, Z. Zou, J. Huang and C. Xu, A Novel MoNi@Ni(OH)$_2$ Heterostructure with Pt-like and Stable Electrocatalytic Activity for the Hydrogen Evolution Reaction, *Chem. Commun.*, 2020, **56**, 1729–1732.

23 E. J. Popczun, C. G. Read, C. W. Roske, N. S. Lewis and R. E. Schaak, Highly Active Electrocatalysis of the Hydrogen Evolution Reaction by Cobalt Phosphide Nanoparticles, *Angew. Chem., Int. Ed.*, 2014, **53**, 5427–5430.

24 M. Jin, Y. Liu, J. Wang, X. Zhang, M. Han, Y. Zhang, G. Wang and H. Zhang, Iron Covalent Doping in WB$_2$ to Boost Hydrogen Evolution Activity, *Inorg. Chem. Front.*, 2022, **9**, 524–530.

25 Y. Song, H. Wang, J. Xiong, B. Guo, S. Liang and L. Wu, Photocatalytic Hydrogen Evolution Over Monolayer H$_{1.07}$Ti$_{1.73}$O$_4$·H$_2$O Nanosheets: Roles of Metal Defects and Greatly Enhanced Performances, *Appl. Catal., B*, 2018, **221**, 473–481.